Improving the Electrochemical Energy Storage Capacity of the Renewable Carbon Derived from Industrial Tea Waste

Ayşenur Karamustafa[a], Sözer Sözer[a], Kürşad Oğuz Oskay[b], Merve Buldu-Akturk[c], Emre Erdem[c], and Gökçen Akgül[a], *

[a] *Department of Energy Systems Engineering, Engineering Faculty, Recep Tayyip Erdogan University, Rize, 53100 Turkey*
[b] *Department of Metallurgy, Engineering Faculty, Cumhuriyet University, Sivas, 58140 Turkey*
[c] *Department of Materials Science and Nano Engineering, Sabancı University, Istanbul, 34956 Turkey*
e-mail: gokcen.akgul@erdogan.edu.tr

Abstract—Energy storage is gaining a vital role since the usage of portable electric/electronic devices and vehicles have been growing. Capacitors, called as electrochemical double layer capacitors or supercapacitors, find application on wide scale devices from mobile vehicles to huge electric vehicles with high energy and power densities, fast charge and discharge properties. Hence, energy is stored at the electrode—electrolyte interface, the electrode material forms the heart of this energy storage system. When the decreasing reserves of fossil resources and their environmental damages are considered, renewable 3-dimentional carbon could be a solution in the capacitor as carbon electrodes. Biomass-derived renewable carbon is cost-effective, abundant, sustainable, safety and environmentally friendly material. In this work, renewable carbon material was derived from industrial tea waste and three methods of graphitization, activation and heteroatom doping were implemented alltogether to develop the energy storage capacity of material. The structural ordering, surface area growth and capacitive contribution promoted the energy storage capacity to 25 F/g and high power density to 2.6 kW/kg of biowaste derived carbon.

INTRODUCTION

Energy is the most important key of modern economies of which demand is increasing by developing living standards and technologies [1]. Correspondingly, energy storage is gaining a vital role since the usage of portable electric/electronic devices and vehicles have been growing. Furthermore, energy generation from renewables is desired for climate and environmental issues and carbon-free energy sources (solar, hydrogen and wind etc.) are required to meet the increasing energy needs.

Storage of energy to ensure energy continuity and portability depends mostly upon the energy storage technologies and material engineering [2, 3]. Differ from hydro, thermal and mechanical energy storage, electrochemical energy storage is the representative for electrical energy storage.

Capacitors, called as electrochemical double layer capacitors (EDLC) or supercapacitors, find application on wide scale devices from mobile vehicles to huge electric vehicles with high energy and power densities, fast charge and discharge properties. Basically, when voltage is applied (charging) to the capacitor consisting of electrode, electrolyte and dielectric plate, the two plates are charged opposite to each other, an electric field is created and energy is stored.

Electrodes are the most important parts that affect the performance in capacitors. Hence, energy is stored at the electrode-electrolyte interface, the electrode material forms the heart of this energy storage system. Metal oxides, polymers and carbon-based materials are used with the varying desired behaviors such as double layer, pseudo-capacitive or faradaic one [4, 5].

Carbon-based materials with the dominant double layer behavior are the interest of recent researches because of carbon's thermal stability, high surface area, porosity and well-electrical conductivity that these provide convenient diffusion and ion transfer by adsorption-desorption of electrolytes, in the end increases the energy storage capacity. The presence of surface functional groups on carbon materials enables chemical sorption and facilitates the diffusion of ions into the pores and even intercalation in the crystalline interlayers resulting in well-wettability [6, 7].

Carbon has various allotropes with different crystal structures in 0–3 dimensions; such as graphite,
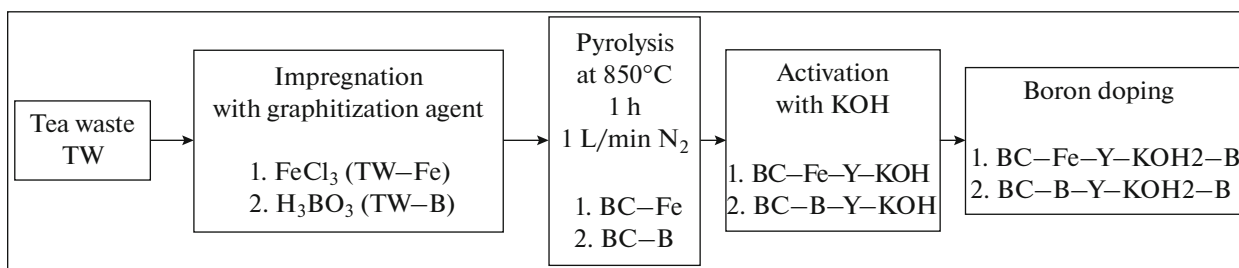
| Tea waste TW | → | Impregnation with graphitization agent

1. FeCl$_3$ (TW–Fe)
2. H$_3$BO$_3$ (TW–B) | → | Pyrolysis at 850°C
1 h
1 L/min N$_2$

1. BC–Fe
2. BC–B | → | Activation with KOH

1. BC–Fe–Y–KOH
2. BC–B–Y–KOH | → | Boron doping

1. BC–Fe–Y–KOH2–B
2. BC–B–Y–KOH2–B |

Fig. 1. The flow chart of the experimental procedure.

graphene, diamond, carbon fiber, activated carbon, carbon black, carbon nanotube, fullerene etc. The different physical and chemical properties of each allotrope diversify the carbon capacitors [8, 9]. Preparation procedures for 0–2 dimension carbon materials (graphene, nanotubes etc.) can be complex and costly [10]. Furthermore, most of such carbon materials are fossil origin. Therefore, 3-dimensional renewable carbon materials are recently being investigated in capacitor applications [6, 11]. When the decreasing reserves of fossil resources and their environmental damages are considered, renewable 3-dimensional carbon could be a solution in the capacitor as carbon electrodes.

The only renewable carbon source is biomass. Biomass-derived renewable carbon is cost-effective, abundant, sustainable, safe and environmentally friendly material [12, 13]. Active centers, surface functional groups and porosity ensure penetration of the electrolyte well into the material that are beneficial for energy storage applications by altering the reaction kinetics and thermodynamics via wettability and electrical conductivity [14–16]. Sun et al. [17] derived porous carbon material from quinoa by alkali activating and carbonization and determined the electrochemical capacitances as 330 F/g at 1 A/g that exhibits remarkable electrochemical performance. Kalpana et al. [18] prepared carbon material from recycled waste paper with a specific capacitance of 160 F/g with 99% coulombic efficiency at a current density of 1 mA/cm^2. Hierarchical porous carbon was prepared from onion peel waste material by pyrolysis without any activation and its electrochemical performance for supercapacitor applications was determined as 127 F/g at the current density of 0.75 A/g in aqueous H$_2$SO$_4$ electrolyte [19].

The disadvantages of such biomass derived carbon materials are mostly their amorphous structure that infers less electrical conductivity. Besides, biomass derived carbon is not pure carbon, contains minerals which can result in impedance in the material. Else, the pore structures are not at the desired level compared to lower dimensional carbons. Despite all these, the properties of this material could be tuned by some activations or modifications for broad usage of capacitors [12, 20].

Physical and chemical activations by treating the biomass derived carbon with steam, acids or bases would improve the surface area and porosity properties for a better ion transferring in the structure. Furthermore, the amorphous carbon skeleton can be converted to the graphene like structures by graphitization, exfoliation or ultrasonic treatments [8, 21–23]. Additionally, the metal-biochar composites develop the ion adsorption on the surface by an electrostatic attraction thus energy storage capacity.

In this work, all three methods of graphitization, activation and heteroatom doping were implemented to develop carbon materials with an improved energy storage capacity for supercapacitor applications by eliminating the general disadvantages of renewable carbon. An enhancement of the physical and chemical properties was established.

EXPERIMENTAL

Preparing of Refined Carbon Materials from Industrial Tea Waste Biomass

The tea waste biomass obtained from a local tea industry in the form of straw (<2.36 mm) was grinded and sieved from 0.5 mm sieve. The dried raw biomass (TW) at 80°C overnight was carbonized according to the experimental flowing procedure given in Fig. 1. Graphitization, activation and heteroatom boron doping are the main stages for obtaining the refined well-capacitance carbon material from tea waste.

At the first stage, two different graphitization agents of FeCl$_3$ and H$_3$BO$_3$ (Tekkim) were impregnated to TW as 2 : 1 (w/w) ratio (TW : Metal compound) separately. The impregnated samples (TW–Fe, TW–B) were dried and then pyrolized in a rotary oven (Protherm RTR 11/100/500) at 850°C for 1 h at the inert atmosphere of N$_2$ with 1 L/min flow rate and ~10°C/min heating rate. After each pyrolysis, the samples were let cool down under continuing N$_2$ flow to room temperature. The produced samples were nomenclatured as BC–Fe and BC–B, then washed with 6 M HCl and 6 M HF to remove the impregnated metal-oxides and the other possible minerals biomass included. Final products were washed with water

(BC−Fe−Y, BC−B−Y). "BC" identifies the carbon samples as biochar.

Activation, the second experimental stage, was performed with KOH aiming to develop the surface area and porosity of the carbon materials. KOH was impregnated to BC−Fe−Y with the various ratios of 1 : 4 (KOH1), 1 : 2 (KOH2) and 4 : 1 (KOH3) (w/w) as carbon : KOH. The impregnated samples were dried at 85°C and pyrolyzed second time at 850°C for 15 min at the inert atmosphere of N_2 with 1 L/min flow rate with a rapid heating rate of ~35°C/min. The 4 : 1 impregnated and pyrolyzed sample (BC−Fe−Y−KOH3) burned itself as soon as it contacted air. The optimum KOH activation ratio was determined as 1 : 2 (KOH2) and applied to BC−B−Y as well. Activated samples were washed after pyrolysis with diluted HCl and water to neutralize them, dried and stored for the next stage. They were nomenclatured as BC−Fe−Y−KOH1, BC−Fe−Y−KOH2 and BC−B−Y−KOH2.

Heteroatom boron was doped with the following procedure in the third step; BC−Fe−Y−KOH2 and BC−B−Y−KOH2 samples as the optimum activated ones were impregnated with saturated aqueous H_3BO_3 solution in 1 : 1 and 2 : 1 (w/w, biochar: boric acid) ratios. The dried samples were heated at 200°C for 3 h to obtain BC−Fe−Y−KOH2-B1/B2 and BC−B−Y−KOH2-B1/B2. H_3BO_3 should turn to boron oxide forms.

Characterizations of Carbon Samples

The structure of the carbon samples was characterized for surface area and pore volumes by BET (QuantachromeAutosorb 1C and Quantachrome Asi Qwin™). The particle size distribution was determined by Malvern Mastersizer 3.60 (refractive index was accepted as 1.746 for all the samples). The XRD (PANalytical/Empreyan X-ray diffractometer non-monochromatographic Cu$K_{\alpha 1}$-radiation (45 kV, 40 mA, λ = 1.54 Å)), SEM (Jeol JSM-6610), TGA (NETZSCH STA 449F3), FTIR (Varian/660-IR) analyses were performed to characterize the carbon samples in detail. pH and electrical conductivities of the samples were determined with a pH meter (Metrohm) with a conductivity probe according to International Biochar Initiative Standards [24].

Electrochemical Analyses

The capacitances of the samples were determined by cyclic voltammetry (CV) using a potentiostat/galvanostat (Gamry Interface 5000E) in the three electrode system; the Pt counting electrode (CE), Ag/AgCl reference electrode (RE) and the glassy carbon working electrode (WE, 0.071 cm^2). The binder material poly(1,1,2,2-tetrafluoroethylene) (PTFE) was mixed with the carbon samples in 20% (w/w) with the aid of methanol and the mixture was sonicated in a sonic bath for a better mixing. The prepared carbon sample was placed on the working electrode surface by dropping. The weight of the dry electrode was measured to determine the weight of the carbon sample. Voltammograms were obtained in the 0−0.8 V potential window and scanning range of 10−500 mV/s in 1 M Na_2SO_4 solution. The CV measurement was additionally performed in 1 M H_2SO_4 for the sample having the best capacitance.

Galvanostatic Charge/Discharge (GCD) measurements were performed over a voltage window of −1 to +1 V at current density of 2.5 A/g on BioLogic VMP 300 electrochemical workstation having potentiostatic electrochemical impedance spectroscopy (PEIS) channel unit. PEIS studies were accomplished by applying a sinusoidal signal of 10 mV from 10 mHz to 1 MHz frequency range. The supercapacitor device design has been done as follows: electrode1: sample, electrode 2: active carbon (Merck, <30 μm particle size), electrolyte: 1 M LiPF$_6$ (Aldrich) in ethylene carbonate and diethyl carbonate (EC : DEC, 1 : 2) and separator: glass fiber (Whatman).

RESULTS AND DISCUSSION

Structural Characterizations of the Carbon Materials

Surface area, porosity and surface functionality are accepted as the main parameters that directly affect the supercapacitor performance. The pores in the carbocous material should be proper for faster ion movement in the well-performance supercapacitors. Ions would appropriately snug fit in the pore structures. The surface areas of the samples derived from industrial tea waste by various methods are given in Table 1. The graphitization treatment with FeCl$_3$ developed the surface area to 579.4 m^2/g. The surface area of pristine biochar as 5.7 m^2/g [25] was improved to 294.1 m^2/g by H_3BO_3 graphitization although both BC−Fe and BC−B samples have lower surface areas probably due to the blockage of the pores by accumulation of the iron and boron oxides emerging during the pyrolysis. This situation was also observed by the heteroatom doping step. The main development of the surface areas and microporosity was attained by KOH activation. Activation of samples exhilarates the surface area to 1372.7 m^2/g with the proper KOH activation ratio for BC−B−Y−KOH2. Heteroatom doping led to decline in the surface area of BC−Fe−Y−KOH2 and BC−Fe−Y−KOH2−B1 from 1316.5 to 118.7 m^2/g, respectively.

The particle size distribution analyses show a particle distribution around ~10 μm. Figure 2 presents the particle size distributions of two samples of BC−B and BC−B−Y−KOH2 which have the smallest and the highest surface areas, respectively. It is seen that the cumulative volume (the number of particles in those sizes) decreases with the development of the surface

Table 1. Surface areas of the samples

Sample	External surface area, m^2/g	Micropore area, m^2/g	Total surface area, m^2/g
BC−Fe	50.3	17.1	67.4
BC−B	7.4	0	7.4
BC−Fe−Y	112.1	467.3	579.4
BC−B−Y	146.8	147.3	294.1
BC−Fe−Y−KOH1	216.4	913.6	1130.0
BC−Fe−Y−KOH2	223.0	1093.5	1316.5
BC−B−Y−KOH2	369.1	1003.7	1372.7
BC−Fe−Y−KOH2−B1	87.0	31.6	118.7
BC−Fe−Y−KOH2−B2	117.6	240.2	357.7
BC−B−Y−KOH2−B1	174.1	54.4	228.5
BC−B−Y−KOH2−B2	197.3	87.6	284.9

Table 2. Heteroatom content (from TGA analyses), pH and electrical conductivity of the samples

Sample	Heteroatom content, %	pH	Electrical conductivity, μS/cm
BC−Fe	36	6.38	6470
BC−B	49	6.33	1580
BC−Fe−Y	8	6.34	387
BC−B−Y	3	6.29	516
BC−Fe−Y−KOH1	−	6.57	10240
BC−Fe−Y−KOH2	−	6.56	15270
BC−B−Y−KOH2	−	6.57	17230
BC−Fe−Y−KOH2−B1	30	6.35	320
BC−Fe−Y−KOH2−B2	20	6.53	268
BC−B−Y−KOH2−B1	50	6.47	231
BC−B−Y−KOH2−B2	41	6.31	75

areas. Generally, the samples do not consist of homogeneous particles.

Thermograms of the BC samples under air atmosphere are given in Fig. 3. TGA analyses indicate that the BC−B and BC−Fe samples contain 49 and 36 wt % mostly B and Fe oxides, respectively. The graphitization agents and possible minerals were removed as a result of washing successfully to 3 and 8 wt % for BC−B−Y and BC−Fe−Y (Fig. 3). The TGA analyses of the activated and heteroatom doped samples are given in Fig. S1 and S2. Except for the BC−B−Y−KOH2 sample, all the samples show similar TGA curves where the weight loss until 200°C ascribes to the loss of moisture, light volatiles and the organic contents started to decompose after 500°C by breaking the chemical bonds. BC−B−Y−KOH2 is quite stable than all other samples would be as a result of higher structural organization [26]. Table 2 summarizes the heteroatom contents obtained from TGA analyses.

The XRD patterns of the graphitization step samples shown in Fig. 4 exhibit two main broad peaks at 24° and 44° 2θ corresponding to the (002) and (101) reflections of carbon. A sharp peak at ~45° (110) and the peaks at 38°−43° of BC−Fe sample could be responsible for the dominant iron oxides in Fe_3O_4 form [27]. Broadly, the other samples have the similar patterns except BC−B−Y−KOH2 (Fig. S3). Various distinctive peaks appearing between 24° and 44° should belong to graphitic and oxidative carbonaceous mixture [28]. It has been observed that KOH also has an effect on the regulation of the crystal structure, but this happens only in carbon graphitized with H_3BO_3 agent. Figure S4 shows the XRD patterns of heteroatom doped samples that possible B_2O_3 peaks could be seen at 15°, 28°, and 40° 2θ [29] especially for the BC−Fe−Y−KOH2-B1 and BC−B−Y−KOH2-B1 samples with higher boroxide contents.

The surface functionality of the samples was determined by FTIR analyses given in Fig. 5, S5−S6. Gen-
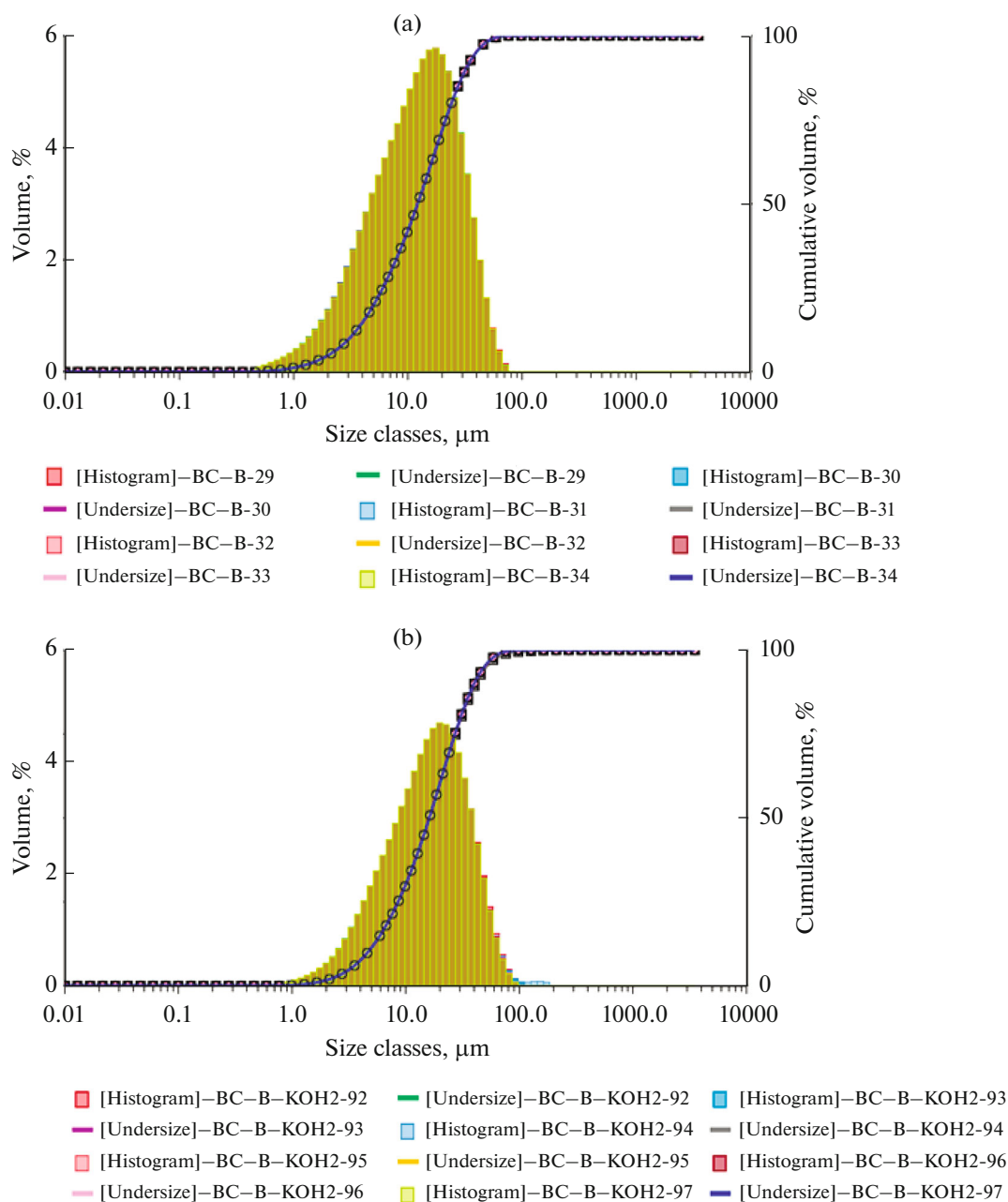
Fig. 2. Particle size distributions of (a) BC−B and (b) BC−B−Y−KOH2.

erally, all samples are rich in oxygen groups on the surface that the peaks such as O−H (wide band ~3400 cm^{-1}), C−O−H (~1450 cm^{-1}), C−O (~1050 cm^{-1}) are abundantly seen in the analyses. Treatment with KOH may have enriched the oxygen groups even more. The aliphatic C−H stretches around 2970 cm^{-1} are also observed. Although not very obvious, the B−O and Fe−O stretching could be determined at ~1200 and ~580 cm^{-1}, respectively [25, 30]. The high oxygen content could help to enhance the wettability with electrolyte solution.

The morphological images (SEM) of the samples are given in Fig. 6, S7. A jagged surface can be seen generally. After the activation of the BC−Fe−Y, structural collapses can be clearly observed (Fig. S7). A structural organization is revealed for the BC−B−Y−KOH2 (Fig. 6). The irregular structure became dominant again after heteroatom doping. The distribution of boron compounds on the surface is also seen in the EDX charts (Fig. S7).

The pH and electrical conductivities are given in Table 2 as well. The pH values are around 6 whereas electrical conductivities vary from 75 to 17 mS/cm.
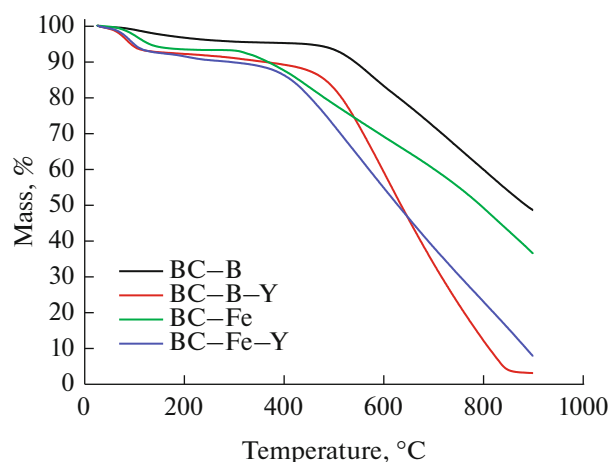
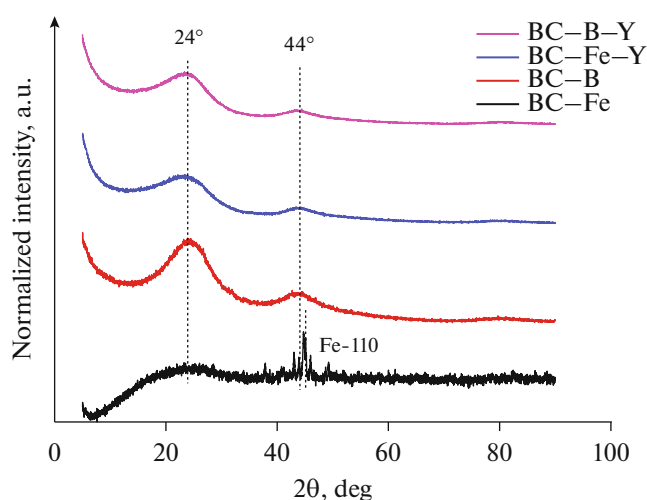**Fig. 3.** TGA analyses of graphitization step samples.

Fig. 5. FTIR results of the samples.

Fig. 4. XRD patterns of graphitization step samples.

Fig. 6. SEM image of BC−B−Y−KOH2.

These magnificent differences should be the result of structural ordering which worked out by the analyses mentioned above. It is assumed that the more ordering the carbon structure results the more electrical conductivity since BC−B−Y−KOH2 has the highest conductivity. On the other hand, iron and boron oxides enhance the electrical conductivity of the carbon samples as well. Iron oxides are desired composite-type and backbone materials for supercapacitors through a better ion-diffusion [31]. As further, boron oxides tune the conductivity of carbon materials by contributing a p-type behavior enforcing and accelerating the electron accepting property [32, 33]. The electrical conductivity contribution of the metal oxides to carbon can be seen for BC−Fe (6.5 mS/cm) and BC−B (1.6 mS/cm) of which conductivities are far higher than BC−Fe−Y (0.4 mS/cm) and BC−B−Y (0.5 mS/cm), respectively. Moreover, the diffusion mechanism could override the p-type behavior for
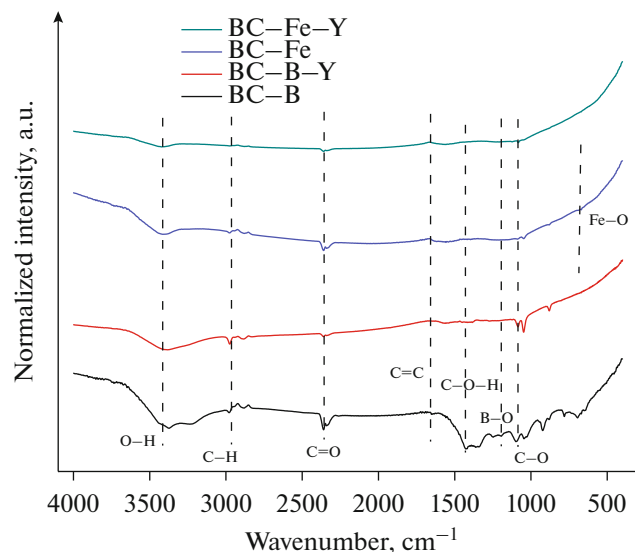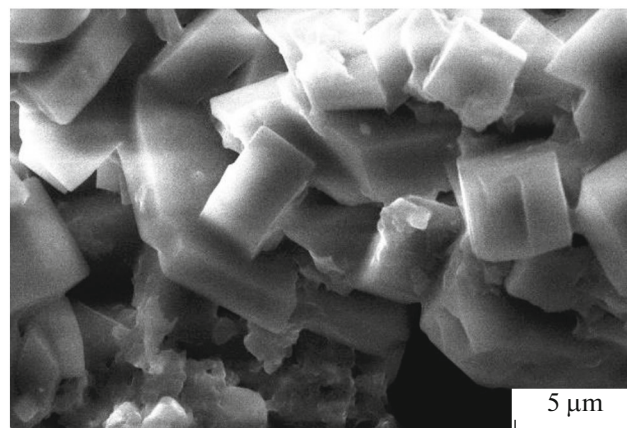
these carbon structures, hence activated samples have higher conductivities.

Electrochemical Characterizations

The specific energy storage capacitances (F/g) of the samples were calculated by Equation (1) via integrating the curve areas of CV analyses (Fig. S8) given in Table 3.

$$C = \frac{1}{2sm\Delta V}\int IVdV, \qquad (1)$$

where s is the scan rate (V/s), m mass of the material (g), ΔV is the potential window (V). The shapes of the CVs give clues about electrochemical behavior of the electrode material. BC−Fe shows more faradaic behavior than other carboceous materials due to pos-
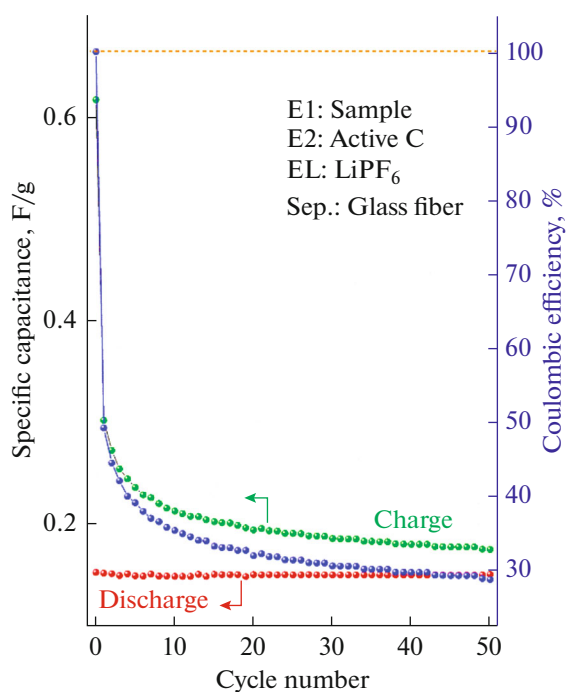
Fig. 7. GCD analysis of BC−B−Y−KOH2−B2.

sible redox potentials of the iron oxides. When the scan rate increases, the specific capacitance value decreases since the size of the diffusion layer shrinks. The surface area and porosity rapturized due to emerging the tailored pores to higher than 1300 m²/g following increased capacity to 20.93 F/g by enhanced ion transfer into the pores. However, BC−B−Y−

KOH2 of which capacitance is very low as 0.78 F/g with the highest surface area of 1372.7 m²/g. This could be the result of better organization of the carbon structure by graphitization and the further activation to the highest electrical conductivity (Table 2).

The capacitance of BC−B−Y−KOH2−B2 in 1 M H₂SO₄ electrolyte was also measured to determine if the ion diameter affects the capacitances with a better penetration to micropores. It was observed, however, BC−B−Y−KOH2−B2 has similar capacitances in neutral (24.98 F/g) and acid (21.27 F/g) environments. It could be shown that the bulk volume would be so large and the ions can move freely without transferring the charge onto the surface.

GCD behavior of the best capacity sample of BC−B−Y−KOH2−B2 is shown in Fig. 7. The capacitance (F/g) at 2.5 A/g current density was evaluated by Equation (2).

$$C = \frac{I\Delta t}{\Delta V m}, \tag{2}$$

where I is the discharge current (A), Δt is the discharge time (s), m mass of the material (g), ΔV is the potential window (V). The capacitance was determined as 0.7 F/g more reliable regarding the charge storage process.

The energy and power densities were calculated by Eqs. (3) and (4) given in Fig. 8.

$$E = \frac{1}{2}C(\Delta V)^2, \tag{3}$$

$$P = \frac{E}{t}, \tag{4}$$

Table 3. Specific capacitances of the samples

| Sample	Capacitances, F/g					
	Scan rates, mV/s					
	10	20	50	100	250	500
BC−Fe	0.35	0.35	0.29	0.23	0.17	0.15
BC−B	0.42	0.36	0.30	0.26	0.22	0.20
BC−Fe−Y	3.73	2.69	1.75	1.25	0.74	0.49
BC−B−Y	1.66	1.33	0.75	0.53	0.33	0.23
BC−Fe−Y−KOH1	19.61	17.06	13.80	11.22	7.67	5.34
BC−Fe−Y−KOH2	20.93	14.04	8.59	5.96	3.41	1.99
BC−B−Y−KOH2	0.79	0.52	0.28	0.17	0.09	0.05
BC−Fe−Y−KOH2−B1	10.72	7.50	5.43	4.03	2.47	1.25
BC−Fe−Y−KOH2−B2	12.53	9.43	5.99	4.18	2.47	1.52
BC−B−Y−KOH2−B1	10.01	7.87	5.18	3.65	2.11	1.27
BC−B−Y−KOH2−B2	24.98	17.00	10.37	7.31	4.26	2.56
BC−B−Y−KOH2−B2 in acid	21.27	15.40	9.78	7.02	4.44	3.07
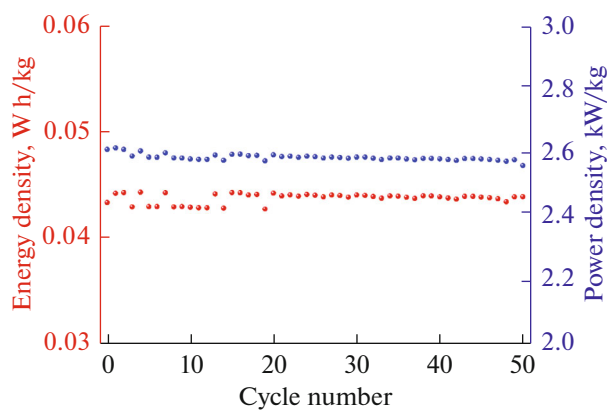
Fig. 8. Energy and power densities of BC−B−Y−KOH2−B2.

where E is energy density (W h/kg), P is power density (kW/kg), t is the discharge time (s), ΔV is the potential window (V). Relatively low energy density (~0.044 W h/kg) was observed but the power density is quite high (~2.6 kW/kg) which is in the range of typical supercapacitors [34]. There are still plenty of rooms to improve the energy density for biowaste (tea) samples.

PEIS is used to investigate the transport properties of porous material BC−B−Y−KOH2−B2 at 10 mHz to 1 MHz frequency range. The Nyquist and Bode plots of BC−B−Y−KOH2−B2 are shown in Fig. 9a. The experimental impedance data was fitted with the equivalent circuit given in Fig. 9c and fitted parameters were calculated. A vertical EIS spectrum at the low frequencies indicates a relative better capacitance
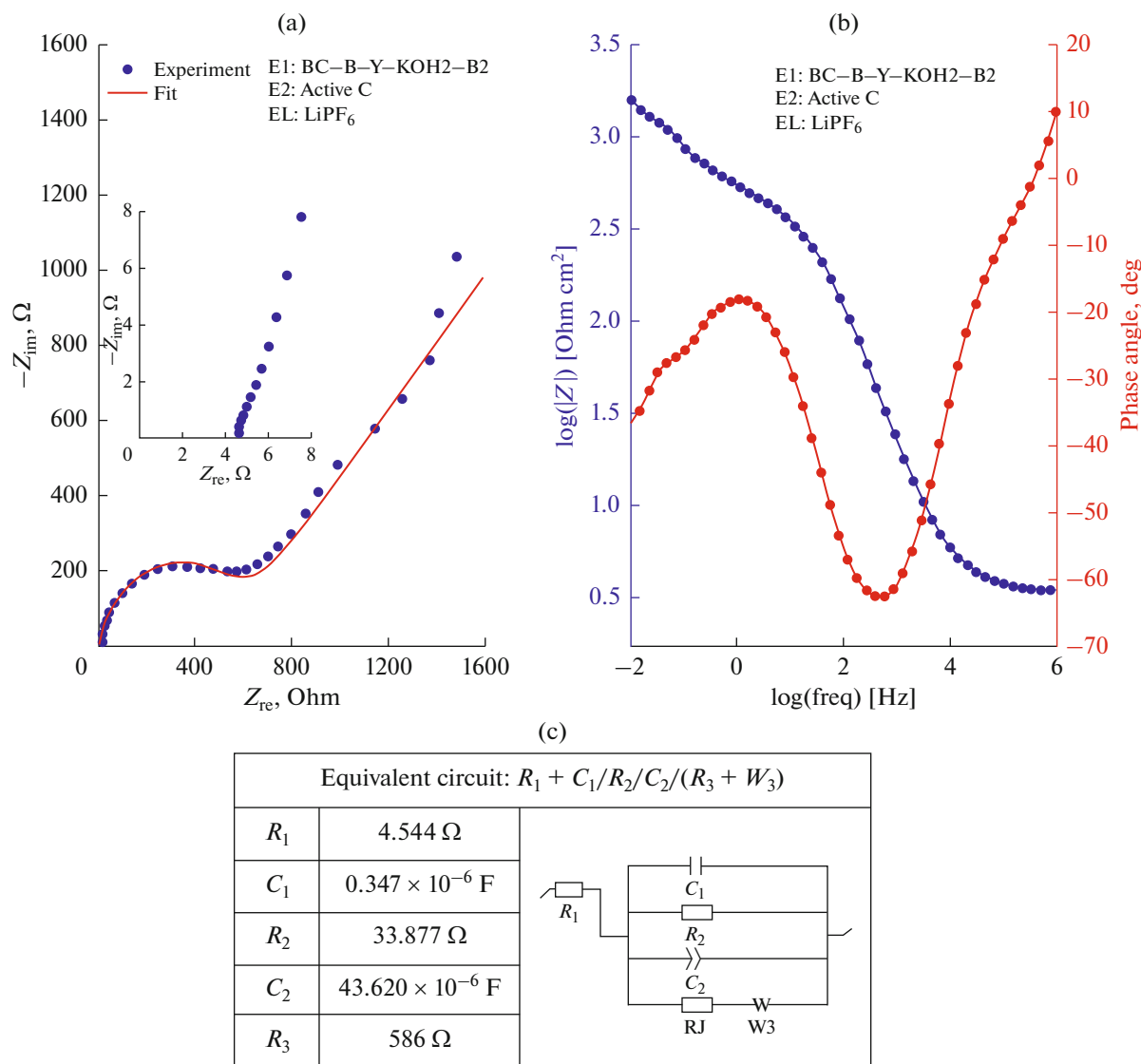

Equivalent circuit: $R_1 + C_1/R_2/C_2/(R_3 + W_3)$	
R_1	4.544 Ω
C_1	0.347 × 10^{-6} F
R_2	33.877 Ω
C_2	43.620 × 10^{-6} F
R_3	586 Ω

Fig. 9. PEIS analysis of BC−B−Y−KOH2−B2. (a) Nyquist plot (inset shows the low frequency region), (b) Bode plot and (c) the equivalent circuit used to fit the experimental impedance data.

Table 4. b values of the samples

| Sample	b	R^2
BC−Fe	0.73	0.994
BC−B	0.89	0.999
BC−Fe−Y	0.78	0.998
BC−B−Y	0.59	0.998
BC−Fe−Y−KOH1	0.75	0.999
BC−Fe−Y−KOH2	0.53	0.997
BC−B−Y−KOH2	0.44	0.999
BC−Fe−Y−KOH2−B1	0.54	0.990
BC−Fe−Y−KOH2−B2	0.52	0.998
BC−B−Y−KOH2−B1	0.55	0.997
BC−B−Y−KOH2−B2	0.48	0.999
BC−B−Y−KOH2−B2 in acid	0.53	0.999

behavior which is due to the diffusion of the electrolyte ions and called the Warburg impedance. The charge transfer between material and electrolyte should increase in the range of $700-1600 \, \Omega$ at higher frequencies appearing as a straight Warburg type line. The ionic diffusion coefficient is related to Warburg element, and it can be estimated using the theoretical calculations [35]. The frequency response of the system was analyzed from the EIS spectra and the Bode plot of BC−B−Y−KOH2−B2 is presented in Fig. 9b. Both the Nyquist and Bode plots showed that the values of the fitted parameters obtained using the equivalent circuit given in Fig. 9c exhibit consistency with the experimental data from Bode plot in both low and high frequency regions.

The charge storage kinetics of the samples were analyzed by Dunn equation [36]. As given in Eq. (5),

the diffusion and capacitive contributions during the energy storage can be evaluated by calculating the value of b:

$$i = av^b, \tag{5}$$

where i is current (A), a and b are constants, v is scan rate (V/s). The b constant can be determined from the slope of $\log(i)$ versus $\log(v)$. Figure 10 shows $\log(i)-\log(v)$ graph for BC−B−Y−KOH2−B2. Table 4 summarizes the b values of the samples calculated at the cathodic peak regimes. The b value of ~0.5 indicates diffusion-controlled charge storage mechanism while the capacitive-pseudocapacitive mechanism would be dominant while the b value approaches 1. The total results are summarized in Fig. 11.
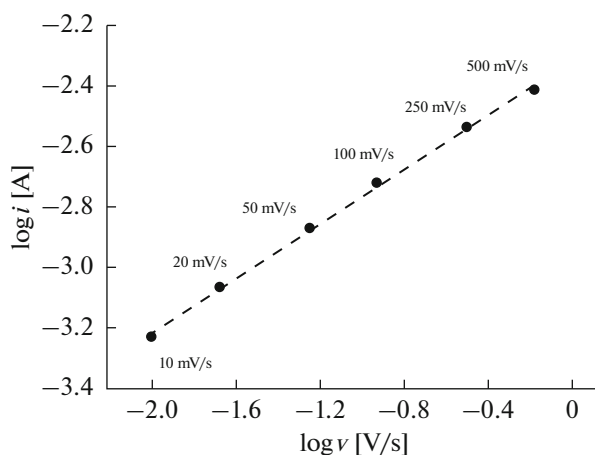
Fig. 10. The determination of b-value of BC−B−Y−KOH2−B2 at cathodic peak regime (linear fitted).
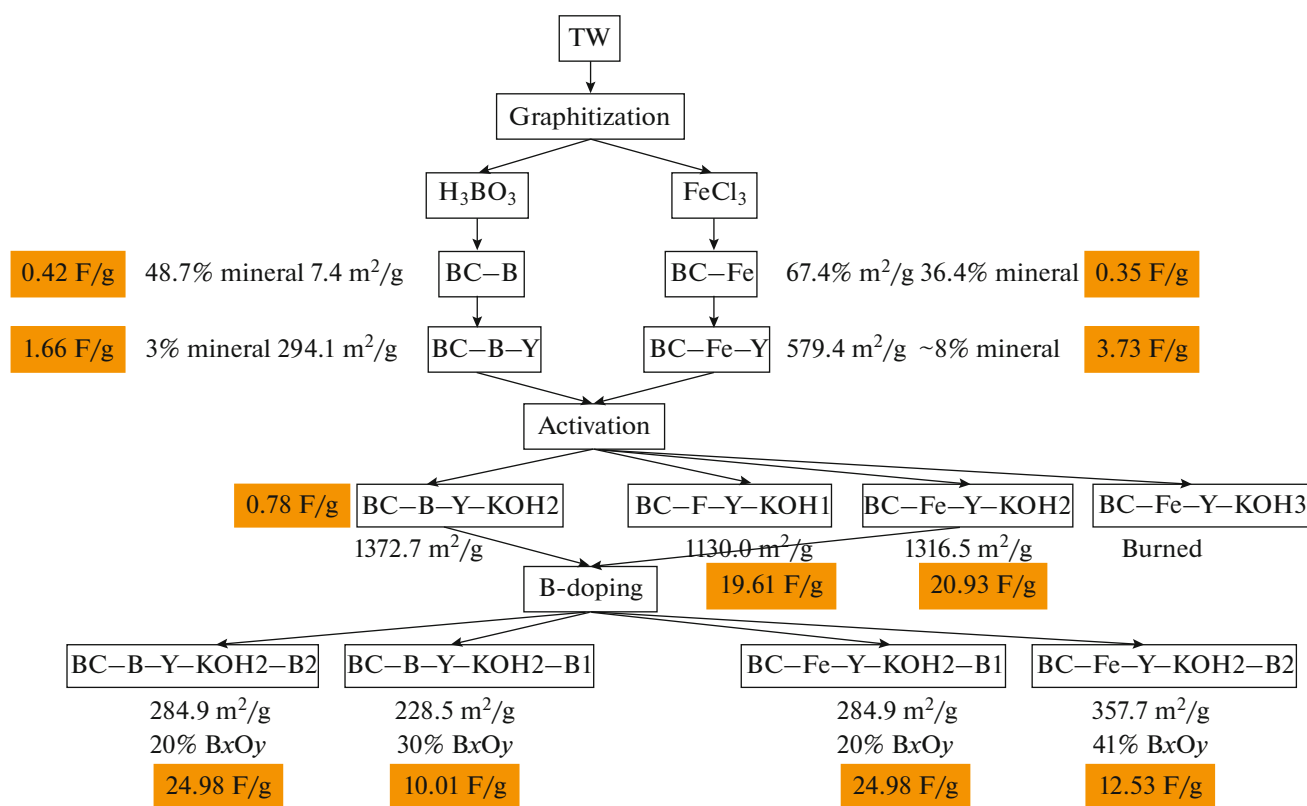
Fig. 11. Total results.

CONCLUSIONS

The electrochemical capacitive properties of tea waste biomass derived carbon material which has mostly amorphous structure, less electrical conductivity and is not at the desired electrochemical capacitive level compared to lower dimensional carbons were tried to develop by three methods of graphitization, activation and heteroatom doping altogether. The capacitive improvement could be achieved. The structural-pore ordering and heteroatom including seem to be important steps for biowaste derived carbon material and this material could be tuned by some activations or modifications for broad usage of capacitors.

FINANCIAL SUPPORT

CONFLICT OF INTERESTS

Authors announce that there is no conflict of interest.

SUPPLEMENTARY INFORMATION

The online version contains supplementary material available at https://doi.org/10.1134/S1023193522090099.

REFERENCES

1. Jacobson, M.Z. and Delucchi, M.A., Providing all global energy with wind, water, and solar power, *Energy Policy,* 2011, vol. 39, p. 1154.

2. Bullich-Massagué, E., Cifuentes-García, F.J., Glenny-Crende, I., Cheah-Mañé, M., Aragüés-Peñalba, M., Díaz-González, F., and Gomis-Bellmunt, O., A review of energy storage technologies for large scale photovoltaic power plants, *Appl. Energy,* 2020, vol. 274, p. 115213.

3. Pomerantseva, E., Bonaccorso, F., Feng, X., Cui, Y., and Gogotsi, Y., Energy storage: the future enabled by nanomaterials, *Science,* 2019, vol. 366, p. eaan8285.

4. Afif, A., Rahman, S.M., Tasfiah Azad, A., Zaini, J.M.A., and Islan Azad, A.K., Advanced materials and technologies for hybrid supercapacitors for energy storage—a review, *J. Energy Storage,* 2019, vol. 25, p. 100852.

5. Pan, Y., Xu, K., and Wu, C., Recent progress in supercapacitors based on the advanced carbon electrodes, *Nanotechnol. Rev.,* 2019, vol. 8, p. 299.

6. Jiang, H., Lee, P.S., and Li, C., 3D carbon based nanostructures for advanced supercapacitors, *Energy Environ. Sci.,* 2013, vol. 6, p. 41.

7. Ratajczak, P., Suss, M.E., Kaasik, F., and Béguin, F., Carbon electrodes for capacitive technologies, *Energy Storage Mater.,* 2019, vol. 16, p. 126.

8. Jiang, L., Sheng, L., and Fan, Z., Biomass-derived carbon materials with structural diversities and their applications in energy storage, *Sci. China Mater.,* 2018, vol. 61, p. 133.

9. Panda, P.K., Grigoriev, A., Mishra, Y.K., and Ahuja, R., Progress in supercapacitors: roles of two dimensional nanotubular materials, *Nanoscale Adv.,* 2020, vol. 2, no. 1, p. 70.

10. Liu, F., Lee, C.W., and Im, J.S., Graphene-based materials for electrochemical energy storage, *J. Nanomater.,* 2013, vol. 2, pp. 107−138, article ID 642915. https://doi.org/10.1155/2013/642915

11. Díez, N., Ferrero, G.A., Fuertes, A.B., and Sevilla, M., Sustainable salt template-assisted chemical activation for the production of porous carbons with enhanced power handling ability in supercapacitors, *Batter. Supercaps.,* 2019, vol. 2, p. 1.

12. Rahman, M.Z., Edvinsson, T., and Kwong, P., Biochar for electrochemical applications, *Green Sustain. Chem.,* 2020, vol. 23, p. 25.

13. Kalyani, P. and Anitha, A., Biomass carbon & its prospects in electrochemical energy systems, *Int. J. Hydrogen Energy,* 2013, vol. 38, p. 4034.

14. Wang, J., Zhang, X., Li, Z., Ma, Y., and Ma, L., Recent progress of biomass-derived carbon materials for supercapacitors, *J. Power Sources,* 2020, vol. 451, p. 227794.

15. Leng, L., Xu, S., Liu, R., Yu, T., Zhuo, X., Leng, S., Xiong, Q., and Huang, H., Nitrogen containing functional groups of biochar: sn overview, *Bioresour. Technol.,* 2020, vol. 298, p. 122286.

16. Tang, W., Zhang, Y., Zhong, Y., Shen, T., Wang, X., Xia, X., and Tu, J., Natural biomass-derived carbons for electrochemical energy storage, *Mater. Res. Bull.,* 2017, vol. 88, p. 234.

17. Sun, Y., Xue, J., Dong, S., Zhang, Y., An, Y., Ding, B., Zhang, T., Dou, H., and Zhang, X., Biomass-derived porous carbon electrodes for high-performance supercapacitors, *J. Mater. Sci.,* 2020, vol. 55, p. 5166.

18. Kalpana, D., Cho, S.H., Lee, S.B., Lee, Y.S., Misra, R., and Renganathan, N.G., Recycled waste paper—a new source of raw material for electric double-layer capacitors, *J. Power Sources,* 2009, vol. 190, p. 587.

19. Mehare, M.D., Deshmukh, A.D., and Dhoble, S.J., Preparation of porous agro-waste-derived carbon from onion peel for supercapacitor application, *J. Mater. Sci.,* 2020, vol. 55, p. 4213.

20. Shrestha, R.G., Maji, S., Shrestha, L.K., and Ariga, K., Nanoarchitectonics of nanoporous carbon materials in supercapacitors applications, *Nanomaterials,* 2020, vol. 10, p. 639.

21. Sizmur, T., Fresno, T., Akgul, G., Frost, H., and Moreno Jiménez, E., Biochar modification to enhance sorption of inorganics from water, *Bioresour. Technol.,* 2017, vol. 246, p. 34.

22. Vijayan, B.L., Misnon, I.I., Kumar, G.M.A., Miyajima, K., Reddy, M.V., Zaghib, K., Karuppiah, C., Yang, C., and Jose, R., Facile fabrication of thin metal oxide films on porous carbon for high density charge storage, *J. Colloid Interface Sci.,* 2020, vol. 562, p. 567.

23. Li, R., Zhou, Y., Li, W., Zhu, J., and Huang, W., Structure engineering in biomass-derived carbon materials for electrochemical energy storage, *Research,* 2020, vol. 2020, p. 8685436.

24. *Standardized Product Definition and Product Testing Guidelines for Biochar, IBI-STD-2.1,* 2015, pp. 1−61. http://www.biochar-international.org/characterization-standard.

25. Akgul, G., Iglesias, D., Ocon, P., and Moreno Jiménez, E., Valorization of tea-waste biochar for energy storage, *Bioenergy Res.,* 2019, vol. 12, p. 1012.

26. Akgül, G., and Bıçakçı, S.N., Optical and electrical properties of refined carbon derived from industrial tea waste, *Mater. Res. Express,* 2020, vol. 7, p. 3.

27. Ruíz-Baltazar, A., Esparza, R., Rosas, G., and Pérez, R., Effect of the surfactant on the growth and oxidation of iron nanoparticles, *J. Nanomater.,* 2015, vol. 2015, p. 240948.

28. Drewniak, S., Muzyka, R., Stolarczyk, A., Pustelny, T., Kotyczka-Morańska, M., and Setkiewicz, M., Studies of reduced graphene oxide and graphite oxide in the aspect of their possible application in gas sensors, *Sensors,* 2016, vol. 16, p. 103.

29. Tran, B.H., Tieu, K., Wan, S., Zhu, H., Cui, S., and Wang, L., Understanding the tribological impacts of alkali element on lubrication of binary borate melt, *RSC Adv.,* 2018, vol. 8, p. 28847.

30. Thirumal, V., Pandurangan, A., Jayavel, R., and Ilangovan, R., Synthesis and characterization of boron doped graphene nanosheets for supercapacitor applications, *Synth. Met.,* 2016, vol. 220, p. 524.

31. Hu, Y., *Carbon and Metal Oxides Based Nanomaterials for Flexible High Performance Asymmetric Supercapacitors,* Singapore: Springer, 2018.

32. Ngidi, N.P.D., Ollengo, M.A., and Nyamori, V.O., Tuning the properties of boron-doped reduced graphene oxide by altering the boron content, *New J. Chem.,* 2020, vol. 44, p. 16864.

33. Prévoteau, A., Ronsse, F., Cid, I., Boeck, P., and Rabaey, K., The electron donating capacity of biochar is dramatically underestimated, *Sci. Rep.,* 2016, vol. 6, p. 32870.

34. Yassine, M. and Fabris, D., Performance of commercially available supercapacitors, *Energies,* 2017, vol. 10, p. 1340.

35. Decaluwe, S.C., Sukeshini, A.M., and Jackson, G.S., Experimental characterization of thin-film ceria solid oxide fuel cell anodes, *ECS Trans.,* 2009, vol. 16, p. 235.

36. Jiang, Y. and Liu, J., Definitions of pseudocapacitive materials: a brief weview, *Energy Environ. Mater.,* 2019, vol. 2, p. 30.